Limnol. Oceanogr., 51(4), 2006, 1581–1593
© 2006, by the American Society of Limnology and Oceanography, Inc.

Modeling vertical excursions of the redox boundary in sediments: Application to deep basins of the Arctic Ocean

Sergei Katsev[1]
Department of Earth and Planetary Sciences, McGill University, 3450 University Street, Montréal, Québec H3A 2A7, Canada

Bjørn Sundby
Department of Earth and Planetary Sciences, McGill University, 3450 University Street, Montréal, Québec H3A 2A7, Canada; and Institut des Sciences de la Mer de Rimouski, Université du Québec à Rimouski, Rimouski, Québec G5L 3A1, Canada

Alfonso Mucci
Department of Earth and Planetary Sciences, McGill University, 3450 University Street, Montréal, Québec H3A 2A7, Canada

Abstract

A diagenetic reaction-transport model was used to simulate how the sediment redox boundary migrates in response to persistent or episodic changes in the deposition flux of degradable organic matter and the concentration of oxygen in the overlying bottom water. The position of the redox boundary is represented by the depth of oxygen penetration. The simulations reveal that the position of the redox boundary in organic-poor sediments, such as those in the deep basins of the Arctic Ocean, is highly sensitive to the flux of organic matter: relatively small and/or brief increases in that flux can cause the redox boundary to migrate rapidly from deep within the sediment to within a few centimeters of the sediment–water interface. Reoxidation of the sediment column after such an event can take years. Redox fluctuations can redistribute solid-phase manganese within the sediment column and produce multiple concentration peaks in its depth profile on a decadal time scale. Manganese peaks observed in sediment cores from the deep basins of the Arctic Ocean do not necessarily correspond to the position of the redox boundary during previous climatic periods or reflect historical changes in manganese deposition rates. The model supports the hypothesis that the recent decrease in the Arctic ice cover has increased the flux of organic matter to the seafloor and moved the redox boundary close to the sediment–water interface. The presence of iron sulfides at depths significantly below the bioturbated layer suggests that either the Arctic sediments have been anoxic for millennia, or iron and sulfate are reduced at these depths by dissolved organic matter diffusing downward from the bioturbation zone.

The redox boundary in aquatic sediments is the depth below the sediment–water interface that separates the stability fields of the oxidized and reduced species of a given redox couple. It is loosely represented by the boundary between oxic and anoxic sediment. The redox boundary is not fixed; it may fluctuate on a variety of time scales in response to such factors as organic matter flux to the sediment surface or oxygen content in the overlying bottom water. Seasonal excursions of the redox boundary often reach several centimeters (Martens and Klump 1984; Glud et al. 2003), and paleorecords suggest even larger migrations in response to climate variability (Mangini et al. 1991; Burdige in press). The differences between the properties of oxidized and reduced species can drive mass fluxes across the redox boundary, redistribute redox elements within the sediment column, and alter the original deposition pattern (Burdige 1993). For example, Gobeil et al. (1997) proposed that the net result of a seasonally fluctuating redox boundary is to separate vertically the zones where, respectively, manganese and cadmium precipitate.

A recent study has shown that the oxic–anoxic boundary in sediments recovered from the deep basins of the Arctic Ocean is located only 2–5 cm below the sediment–water interface (Gobeil et al. 2001). On the basis of discordant vertical distributions of rhenium and acid-volatile sulfide (AVS) in these sediments, Gobeil et al. (2001) proposed that the redox boundary moved to its present position from deep within the sediment column (>40 cm) over the last 50 yr, possibly as a result of an increased flux of degradable organic matter to the seafloor. They also suggested that the redox boundary may have migrated several times during the last several thousand years.

[1] Corresponding author (sergei@eps.mcgill.ca).

Acknowledgments

This research was funded by the Natural Science and Engineering Council of Canada (NSERC) through a Postdoctoral Fellowship to S.K. and Discovery and CASES Network program grants to B.S. and A.M. The numerical code LSSE-Mega was developed by S.K. in collaboration with Dr. Ivan L'Heureux and Benoit Valiron in the framework of the NSERC funded Lake Sediment Structure and Evolution (LSSE) project. We thank Ronnie Glud, David Burdige, and two anonymous reviewers for their incisive and helpful comments on a previous version of the manuscript.

Evidence of past excursions of the redox boundary may be found in the distribution of redox-sensitive elements in the sediment column. In sediment cores from the Arctic shelf, vertical profiles of solid-phase manganese are characterized by a single peak located near the sediment–water interface. In contrast, in the deep basins of the Arctic Ocean, manganese profiles display two or more additional centimeter-scale peaks located 10–20 cm below the sediment surface (Gobeil et al. 2001). Similar multiple peaks of solid Mn were observed in other deep-sea sediments at both high and low latitudes (e.g., Mangini et al. 1991; Burdige in press), as well as in freshwater sediments (Schaller et al. 1997). Because steady-state diagenesis generates a single Mn peak in a narrow depth interval immediately above the redox boundary, Thomson et al. (1996) and Mangini et al. (2001) suggested that multiple Mn peaks in modern sediments may originate from vertical fluctuations of the sediment redox boundary. Estimates based on the magnitudes of the upward fluxes of dissolved Mn suggest that such peaks could accumulate following a redox-boundary migration on the time scale of 10^3–10^4 yr, possibly in a Glacial–Holocene transition (Mangini et al. 2001; Burdige in press). Wilson et al. (1986) proposed that peaks in the profiles of other redox-sensitive elements, which were depth correlated with those of Mn, had a similar origin. Formation of such peaks in response to redox boundary migrations on decadal or seasonal time scales has not yet been subjected to quantitative analysis.

In this study, we use a diagenetic reaction-transport model to chart the position of the sediment redox boundary both in the steady state and in the course of seasonal and decadal variations in response to the flux of degradable organic matter to the seafloor (c.f. Soetaert et al. 1996; Gehlen et al. 1997; Boudreau et al. 1998). The parameterization of the model is adjusted to simulate redox boundary excursions and the ensuing redistribution of solid-phase manganese in the sediments of the deep basins of the Arctic Ocean. The results of this study are not limited to Arctic sediments but apply, at least qualitatively, to other types of aquatic sediments subjected to variations in carbon and oxygen fluxes.

Redox boundary migrations in sediments

The depth of oxygen penetration varies temporally in lacustrine (Carignan and Lean 1991), estuarine (Benoit et al. in press), and marine sediments (Wilson et al. 1986; Gobeil et al. 1997). The most common causes are variations in temperature, bottom-water oxygen concentration, and the flux of degradable organic matter to the sediment surface. Epipelic photosynthesis (Carlton and Wetzel 1988), turbidite or sapropel burn-down (Gehlen et al. 1997; Jung et al. 1997), or leaking of oxygen from aquatic plant roots (Mendelssohn et al. 1995; Sundby et al. 2003) may also be involved.

In deep-sea sediments at midlatitudes, the temporal variability of redox conditions is usually negligible, although organic carbon mineralization rates and benthic oxygen fluxes have occasionally been found to correlate with seasonal differences in the reactivity and flux of organic carbon (Sayles et al. 1994; Soetaert et al. 1996). In the Arctic, however, where the supply of organic matter to the seafloor is not only strongly seasonal (e.g., Hargrave et al. 2002) but also sensitive to climate change (due to the variations in the extent of ice cover), larger displacements of the redox boundary can be expected.

A number of important diagenetic characteristics, such as the fluxes of metals and nutrients within the sediment and across the sediment–water interface, depend on the position of the redox boundary. It is therefore important to determine the factors that control vertical excursions of the redox boundary and the time scales over which the redox boundary responds to these factors. We approach this problem with a generic diagenetic model calibrated to conditions typically found in Arctic deep-sea sediments.

The model

Our reaction-transport model (numerical code LSSE-Mega is available by email from the corresponding author) solves a set of diagenetic equations (Berner 1980; Boudreau 1997) for the concentrations C_i of several solid (in mol per g of dry sediment) and dissolved (in mol L^{-1}) chemical species in the sediment:

$$\frac{\partial \xi C_i}{\partial t} = \frac{\partial}{\partial x}\left(\xi D_i \frac{\partial C_i}{\partial x}\right) - \frac{\partial}{\partial x}(\xi U C_i) + \xi \alpha_{irr}(x)\left(C_i^0 - C_i\right) + \sum_j \xi R_j \quad (1)$$

where t is time and x is the depth coordinate from the sediment–water interface. U is the advection (burial) velocity, and R_j are the rates of relevant chemical and biochemical reactions (for species, reactions, and rates see Tables 1 and 2). The factor ξ is equal to the sediment porosity φ for the dissolved species and to $(1 - \varphi)\rho$ for the solid species, where ρ is the density of dry sediment in g cm^{-3}. D_i is the effective diffusion coefficient calculated as the sum of the bioturbation coefficient D_b and the appropriate molecular diffusion coefficient. The latter is corrected for temperature $T = 5°C$ using expressions in Boudreau (1997), and for sediment tortuosity by an Archie's factor of $\varphi^{1.14}$ (Boudreau 1997). The coefficient $\alpha_{irr}(x)$ describes bioirrigation, and C_i^0 is the dissolved substance concentration at the sediment–water interface.

The boundary conditions at the sediment–water interface are imposed concentration for the dissolved species,

$$C_i(x = 0,t) = C_i^0(t) \quad (2)$$

and imposed-flux for the solid species,

$$-\xi D_i \frac{\partial C_i}{\partial x} + \xi U C_i = F_i^0(t) \quad (3)$$

where F_i^0 is the solid substance flux (in mol cm^{-2} sed yr^{-1}). A no-gradient boundary condition is used for all species at the bottom of the integration domain (x = 20 cm).

Table 1. Model reactions. Notes: S- denotes an adsorption site on a solid substrate surface; R' is dissolution rate.

No.		Rate
	Primary redox reactions	
1	$(CH_2O)_x(NH_3)_y + (x + 2y)\ O_2 \rightarrow x\ CO_2 + y\ NO_3^- + y\ H^+ + (x + y)\ H_2O$	R_{O2}
2	$(CH_2O)_x(NH_3)_y + 4x/5\ NO_3^- \rightarrow x/5\ CO_2 + 4x/5\ HCO_3^- + 2x/5\ N_2 + y\ NH_3 + 3x/5\ H_2O$	R_{NO3}
3	$(CH_2O)_x(NH_3)_y + 2x\ MnO_2 + (3x + y)\ CO_2 + (x + y)\ H_2O \rightarrow 2x\ Mn^{2+} + (4x + y)\ HCO_3^- + yNH_4^+$	R_{MnO2}
4	$(CH_2O)_x(NH_3)_y + 4x\ Fe(OH)_3 + 7x\ CO_2 \rightarrow 4x\ Fe^{2+} + 8x\ HCO_3^- + y\ NH_3 + 3x\ H_2O$	$R_{Fe(OH)3}$
5	$(CH_2O)_x(NH_3)_y + x/2\ SO_4^{2-} \rightarrow x\ HCO_3^- + x/2\ H_2S + y\ NH_3$	R_{SO4}
6	$(CH_2O)_x(NH_3)_y \rightarrow x/2\ CH_4 + x/2\ CO_2 + y\ NH_3$	R_{CH4}
	Secondary redox reactions	
7	$4\ Fe^{2+} + O_2 + 8\ HCO_3^- + 2\ H_2O \rightarrow 4\ Fe(OH)_3 + 8\ CO_2$	R_{FeOx}
8	$4\ S\text{-}Fe^+ + O_2 + 4\ HCO_3^- + 6\ H_2O \rightarrow 4\ S\text{-}H^0 + 4\ Fe(OH)_3 + 4\ CO_2$	R_{surFe}
9	$S\text{-}Mn^+ + 1/2\ O_2 + HCO_3^- \rightarrow S\text{-}H^0 + MnO_2 + CO_2$	R_{surMn}
10	$H_2S + 2\ O_2 + 2\ HCO_3^- \rightarrow SO_4^{2-} + 2\ CO_2 + 2\ H_2O$	R_{SOx}
11	$NH_4^+ + 2\ O_2 + 2\ HCO_3^- \rightarrow NO_3^- + 2\ CO_2 + 3\ H_2O$	R_{NH4Ox}
12	$FeS + 2\ O_2 \rightarrow Fe^{2+} + SO_4^{2-}$	R_{FeSOx}
13	$2\ Fe^{2+} + MnO_2 + 4\ H_2O \rightarrow 2\ Fe(OH)_3 + Mn^{2+} + 2\ H^+$	R_{FeMnO2}
14	$MnO_2 + HS^- + 3\ H^+ \rightarrow Mn^{2+} + S^0 + 2\ H_2O$	R_{MnO2S}
15	$2\ Fe(OH)_3 + H_2S + 4CO_2 \rightarrow 2\ Fe^{2+} + S^0 + 4\ HCO_3^- + 2\ H_2O$	R_{SFe3}
16	$FeCO_3 + H_2S \rightarrow FeS + CO_2 + H_2O$	R_{SFeCO3}
17	$FeS + H_2S \rightarrow FeS_2 + H_2.$	R_{FeSHS}
18	$2\ Fe(OH)_3 + FeS + 6\ CO_2 \rightarrow 3\ Fe^{2+} + S^0 + 6\ HCO_3^-$	R_{FeSFe3}
19	$4\ MnO_2 + FeS + 8\ H^+ \rightarrow 4\ Mn^{2+} + SO_4^{2-} + Fe^{2+} + 4\ H_2O$	R_{FeSMn}
	Mineral precipitation reactions	
20	$Fe^{2+} + HCO_3^- + HS^- \leftrightarrow FeS + CO_2 + H_2O$	R_{FeS}/R'_{FeS}
21	$x\ Mn^{2+} + (1-x)\ Ca^{2+} + 2\ HCO_3^- \leftrightarrow Mn_xCa_{(1-x)}CO_3 + CO_2 + H_2O$ (x=0.95)	R_{MnCO3}/R'_{MnCO}
22	$x\ Fe^{2+} + (1 - x)\ Ca^{2+} + 2\ HCO_3^- \leftrightarrow Fe_xCa_{(1-x)}CO_3 + CO_2 + H_2O$ (x = 1)	R_{FeCO3}/R'_{FeCO3}
	Equilibrium reactions	
	Adsorption	Equilibrium constants
23	$S\text{-}H^0 + Mn^{2+} + HCO_3^- \leftrightarrow S\text{-}Mn^+ + CO_2 + H_2O$	K_{adsMn} (see text)
24	$S\text{-}H^0 + Fe^{2+} + HCO_3^- \leftrightarrow S\text{-}Fe^+ + CO_2 + H_2O$	K_{adsFe} (see text)
	Acid-base reactions	
25	$CO_2\ (aq) + H_2O \leftrightarrow HCO_3^- + H^+$	$K'_{C1} = [H^+][HCO_3^-]/[CO_2]$
26	$HCO_3^- \leftrightarrow CO_3^{2-} + H^+$	$K'_{C2} = [H^+][CO_3^{2-}]/[HCO_3^-]$
27	$H_2S \leftrightarrow HS^- + H^+$	$K'_{HS} = [H^+][HS^-]/[H_2S]$
28	$NH_4^+ \leftrightarrow NH_3 + H^+$	$K'_{NH} = [H^+][NH_3]/[NH_4^+]$
29	$H_2O \leftrightarrow H^+ + OH^-$	$K_W = [H^+][OH^-]$

The decomposition of two different pools of sedimentary organic matter (reactive OM1 and refractory OM2) by the conventional sequence of electron acceptors (Froelich et al. 1979) is assumed to proceed according to Monod kinetics (Table 2). The inhibition constants C_j^{in} characterize the oxidant concentrations above which the less energetically favorable oxidants are inhibited (Boudreau 1997). For simplicity, they are assumed equal to the Monod half-saturation constants for the respective species $C_j^{\lim}$. The secondary redox reactions (Table 1) are assumed to be second order (Table 2) (Van Cappellen and Wang 1996). The rates of precipitation and dissolution reactions are proportional to their respective supersaturations or undersaturations (Table 2).

The pH-dependent adsorption of Mn(II) and Fe(II) ions onto solid sediment phases is described by equilibrium-partitioning coefficients (Van Cappellen and Wang 1996) approximated by Langmuir isotherms:

$$K_{adsFe} = \sum_i \frac{\beta K^*_{Fe\_i} X_i S_{Ti}}{[H^+] + K^*_{Fe\_i}[Fe^{2+}] + K^*_{Mn\_i}[Mn^{2+}]} \quad (4)$$

$$K_{adsMn} = \sum_i \frac{\beta K^*_{Mn\_i} X_i S_{Ti}}{[H^+] + K^*_{Fe\_i}[Fe^{2+}] + K^*_{Mn\_i}[Mn^{2+}]} \quad (5)$$

Here, the summation accounts for total adsorption onto three different substrates: Mn oxides; Fe oxyhydroxides; and a background solid, which collectively represents all other sediment solid surfaces. The constants $K^*_{\mathrm{Fe\_i}}$ and $K^*_{\mathrm{Mn\_i}}$ characterize adsorption of the corresponding ions on the ith substrate, S_{Ti} is the total concentration of sorption sites on the substrate surface (mol of sites per gram of substrate), X_i is the substrate mass fraction in the sediment,

Table 2. Reaction rate expressions used in the model.

Primary redox reactions

For $i,j=\{O_2, NO_3, MnO_2, Fe(OH)_3, SO_4\}$,

$R_i = (k_{OM\ 1}[OM1] + k_{OM\ 2}[OM2])f_i$,

where $f_i = \dfrac{C_i}{C_i + C_i^{\lim}} \Pi_{j=1}^{i-1} \dfrac{C_j^{in}}{C_j + C_j^{in}}$, $f_{CH_4} = 1 - \sum_{j=1}^{5} f_j$

Secondary redox reactions

$R_{FeOx}\ k_{FeOx}[Fe^{2+}][O_2]$

$R_{SOx}=k_{SOx}[TS][O_2]$, where $[TS]=[H_2S]+[HS^-]$

$R_{NH4Ox}=k_{NH4Ox}[TN][O_2]$, where $[TN]=[NH_4^+]+[NH_3]$

$R_{SFe3}\ k_{SFe3}[TS][Fe(OH)_3]$

$R_{SFeCO3}=k_{SFeCO3}[TS][FeCO_3]$

$R_{FeSOx}=k_{FeSOx}[FeS][O_2]$

$R_{surFe}=k_{surFe}[ads-Fe][O_2]$

$R_{surMn}=k_{surMn}[ads\text{-}Mn][O_2]$

$R_{FeSHS}=k_{FeSHS}[FeS][TS]$

$R_{MnO2S}=k_{MnO2S}[MnO_2][TS]$

$R_{Fe3FeS}=k_{Fe3FeS}[Fe(OH)_3][FeS]$

$R_{FeSMn}=k_{FeSMn}[MnO_2][FeS]$

$R_{FeMnO2}=k_{FeMnO2}[Fe^{2+}][MnO_2]$

Mineral precipitation reactions

$R_{FeS}=k_{FeS}(\Omega_{FeS}-1)\delta(\Omega_{FeS}-1)$

$R'_{FeS}=k'_{FeS}[FeS](1-\Omega_{FeS})\delta(1-\Omega_{FeS})$

where $\Omega_{FeS} = \dfrac{[Fe^{2+}_{diss}][HS^-]}{K'_{FeS}[H^+]}$ and $[HS^-] = \dfrac{[TS]}{1 + [H^+]/K'_{HS}}$

$R_{FeCO3}=k_{FeCO3}(\Omega_{FeCO3}-1)\delta(\Omega_{FeCO3}-1)$

$R'_{FeCO3}=k'_{FeCO3}[FeCO_3](1-\Omega_{FeCO3})\delta(1-\Omega_{FeCO3})$

$R_{MnCO3}=k_{MnCO3}(\Omega_{MnCO3}-1)\delta(\Omega_{MnCO3}-1)$,

where $\Omega_{FeCO3} = \dfrac{[Fe^{2+}][CO_3^{2-}]}{K'_{FeCO3}}$, $\Omega_{MnCO3} = \dfrac{[Mn^{2+}][CO_3^{2-}]}{K'_{MnCO3}}$

Here, $\delta(x)=1$ for $x>0$ and $\delta(x)=0$ for $x\leq 0$.

and $\beta = \rho(1 - \varphi)/\varphi$ is the unit conversion factor between solid and dissolved species.

The depth dependence of the bioturbation coefficient, $D_b(x)$, is approximated by

$$D_b = D_b^0 \frac{1 - \tanh((x - H)/\tau)}{1 - \tanh(-H/\tau)} \tag{6}$$

where D_b^0 is the value at the sediment surface, $H = 5$ cm is the location of the steepest gradient within the sediment, and $\tau = 2$ cm is the characteristic depth half-interval where most of the decrease in D_b occurs (Fig. 1). Equation (6) is convenient because, for $\tau = 0$, it transforms into a commonly used step-function approximation, whereas for $H = 0$, it is similar to an approximation of an exponentially decreasing $D_b(x)$ (Boudreau 1997). The bioirrigation coefficient for the dissolved species is approximated (Boudreau 1997) by

$$\alpha_{irr}(x) = \alpha_{irr}^0 \exp(-\alpha_1 x), \tag{7}$$

where parameters α_{irr}^0 and α_1 describe the bioirrigation intensity at the interface and its depth attenuation, respectively. Porosity decreases exponentially with depth from 0.89 at the sediment–water interface to roughly 0.8 at $x = 10$ cm and below (Fig. 1).

Equation 1 with boundary conditions Eqs. 2 and 3 was discretized on an evenly spaced grid of 400 nodes for $0 < x < 20$ cm and solved using a method-of-lines numerical integrator, VODE (Brown et al. 1989), to simulate the evolution of sediment species concentrations in both space and time. Total analytical variables were used to characterize the aqueous concentrations of pore-water carbonate, sulfide, and alkalinity, respectively:

$$[TC] = [CO_2] + [HCO_3^-] + [CO_3^{2-}] \tag{8}$$

$$[TS] = [HS^-] + [H_2S] \tag{9}$$

$$[ALK] = [HCO_3^-] + 2[CO_3^{2-}] + [HS^-] - [NH_4^+] + \beta[ads - Fe] + \beta[ads - Mn] - [H^+] + [OH^-] \tag{10}$$

Here, the terms containing adsorbed species concentrations [ads−Fe] and [ads−Mn] (in mol g^{-1}) account for the release of H^+ in reactions 23 and 24 (Table 1). Assuming local chemical equilibrium, the amounts of Fe(II) and Mn(II) were calculated from total (dissolved + adsorbed) quantities:

$$[t - Fe] = [Fe^{2+}] + [ads - Fe]\beta = [Fe^{2+}](1 + \beta K_{adsFe}) \tag{11}$$

$$[t - Mn] = [Mn^{2+}] + [ads - Mn]\beta = [Mn^{2+}](1 + \beta K_{adsMn}) \tag{12}$$

Because $[H^+]$ is linked to [ads−Fe] and [ads−Mn] through Eqs. 4, 5, and 10, the pore-water $[Fe^{2+}]$, $[Mn^{2+}]$, and $[H^+]$ were calculated at each iteration step from [ALK], [t−Fe], and [t−Mn] with a Newton–Raphson method by solving Eqs. 4–5 and 10–12 together with the equilibrium relationships reported in Table 1.

Kinetic and equilibrium parameters for the model reactions (Table 3) were taken from the dSED online database (Katsev et al. 2004). The acid–base equilibrium constants were calculated for a temperature of 5°C, a salinity of 35, and a water depth of 4,000 m using the expressions of Millero (1995). A sedimentation rate, $U = 0.001$ cm yr^{-1}, typical of deep Arctic sediments at the water depths of interest (Schneider et al. 1996; Middelburg et al. 1997), was selected. Based on correlations with sedimentation rate (Boudreau 1997), we chose a bioturbation coefficient $D_b = 0.1$ cm^2 yr^{-1}. The value of the bioirrigation coefficient ($\alpha_{irr} = 10$ yr^{-1}) is chosen at the lower end of the typical range for aquatic sediments (Boudreau 1997), consistent with the low activity of benthos in deep Arctic sediments (Clough et al. 1997).

The organic matter decay constants (k_{OM1} and k_{OM2}) and the sedimentation fluxes for organic matter (F_{OM1} and F_{OM2}) and manganese oxide (F_{MnO2}) were selected to reproduce (within the variability) the organic carbon and solid-phase manganese profiles of Gobeil et al. (2001) using a steady-state model (Fig. 2, see caption). The value

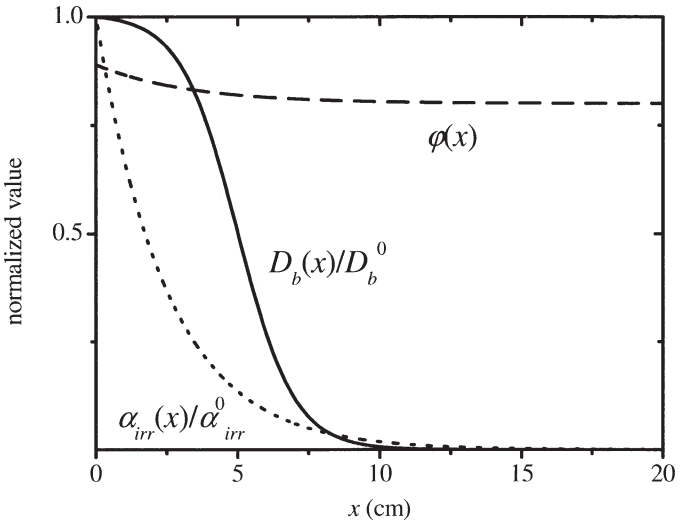

Fig. 1. Depth dependence of the bioturbation coefficient $D_b(x)$, the bioirrigation coefficient $\alpha_{irr}(x)$, and the porosity $\varphi(x)$. $D_b(x)$ and $\alpha_{irr}(x)$ are normalized by their values at the sediment–water interface, D_b^0 and α_{irr}^0, respectively.

obtained for the reactive OM fraction, $k_{OM1} = 0.1$ yr^{-1} (Table 3), is consistent with the concept that a substantial fraction of deposited organic matter is mineralized within several years (Boudreau 1997). Because our model includes only two organic matter fractions, the rate-constant value for the second OM fraction, $k_{OM2} = 4 \times 10^{-5}$ yr^{-1}, represents an effective average for the reactivity of a weakly reactive fraction (with typical value in deep sea sediments about 5×10^{-3} yr^{-1} [Boudreau 1997]) and an OM fraction that does not decompose on the time scales of early diagenesis ($<10^{-8}$ yr^{-1}). This approximation is inconsequential, however, for sediment dynamics on the time scales of years and decades considered here. The total organic carbon flux ($F_{OM1} + F_{OM2}$) in our model is consistent with estimates reported elsewhere (Tromp et al. 1995; Soltwedel et al. 2000; Belicka et al. 2002). Figure 2 illustrates the steady-state model sensitivity to variations in key parameters.

Results and discussion

Position and rate of migration of the redox boundary—In this section, we illustrate the factors that determine the position of the redox boundary in sediment and the rate at which it migrates after an episodic increase in the sedimentation rate of organic carbon. When the benthic oxygen flux exceeds the reducing capacity of the sediment, oxygen can diffuse from the sediment–water interface (SWI) down to an unlimited depth, given sufficient time. Lower rates of oxygen supply or higher contents of reactive organic carbon limit the oxygen penetration depth (OPD) to finite depths. This is illustrated in Fig. 3, which shows the steady-state OPD as a function of the sedimentation flux of reactive organic carbon (F_{OM1}) for different concentrations of oxygen in the overlying water (c.f. Tromp et al. 1995; Mangini et al. 2001). The data in Fig. 3 were obtained using the parameter set in Table 3. For high organic matter fluxes, such as F_3 in Fig. 3, the position of the redox boundary is relatively insensitive to changes in the carbon flux. However, when the carbon flux and, by inference, the concentration of reactive organic carbon in the sediment are low, variations in the organic carbon flux can lead to dramatic excursions of the OPD. For example, with 200 μmol L^{-1} oxygen in the overlying water, increasing the OM sedimentation rate from F_1 to F_2 (Fig. 3) would shift the redox boundary from an infinite depth to within 5 cm of the SWI.

Because oxygen is consumed by bacterial metabolism but supplied by diffusion, the redox boundary can move up much faster than it can move down. Figure 4 illustrates how the OPD evolves after a short pulse in the organic matter flux. The OPD migrates to the sediment–water interface within several years of the increase in F_{OM1} (*see* Fig. 4 caption), whereas the downward migration takes several decades. The rate of migration of the OPD depends on the amounts and reactivities of organic carbon and reduced inorganic substances at a given depth and, thus, varies within the sediment column (Fig. 4). Sedimentary Fe(II), Mn(II), and sulfide, which can consume oxygen, impede the downward migration of the redox boundary. The longer the anoxic conditions persist after the initial upward migration and the greater the amount of reduced species that accumulate, the longer the recovery time. Although the oxygen-concentration gradient decreases with depth, the downward migration rate of the OPD accelerates below the bioturbation zone ($x > 7$ cm in our simulations; Fig. 1), where oxygen consumption rate is slow because of the absence of fresh reactive organic matter.

The results in Figs. 3 and 4 suggest that the organic-poor sediments of the deep Arctic Ocean are prone to large excursions of the redox boundary. An episodic increase in the flux of organic carbon can quickly bring the OPD upward but, depending on the excess amount of metabolizable carbon delivered to the sediment, it could take from several years to several decades to return the oxygen penetration depth to below 20 cm. Figure 5 illustrates the temporal evolution of depth profiles of dissolved oxygen, total solid-phase manganese (oxides, carbonates, and sorbed Mn(II)), ferric iron, and FeS after an increase in the OM flux to the seafloor. To simulate non–steady-state conditions, the flux of reactive organic carbon F_{OM1} was increased from its steady-state value F_1, at $t = 0$, to $10F_1$, for a period of 2 yr. This increase in F_{OM1} triggered a greater oxygen demand in the surface sediment and brought the redox boundary from an infinite depth to within 2.5 cm of the SWI in less than 2 yr. The ensuing anoxic conditions led to the reduction of manganese oxides, iron oxyhydroxides, and sulfate. As the excess reactive organic matter burned down, the redox boundary moved from $x = 2.5$ cm to below 10 cm in approximately 50 yr.

Despite the production of a noticeable amount of iron sulfide (Fig. 5), the rate of sulfate diffusion from the overlying water was sufficient to maintain a nearly constant concentration of pore-water sulfate (not shown) throughout the sediment column. This illustrates that the absence of sulfate reduction cannot be ascertained solely from the

Table 3. Parameter values used in the model. Interface solute concentrations and solid sedimentation fluxes not listed here are zero. References: (a) Tromp et al. (1995), (b) Soltwedel et al. (2000), (c) Boudreau et al. (1998), (d) Boudreau (1997), (e) Berg et al. (2003), (f) Van Cappellen and Wang (1996), (g) Fossing et al. (2004), (h) Hunter et al. (1998), (i) Stumm and Morgan (1996), (j) Morse et al. (1987), (k) Schneider et al. (1996), (l) Middelburg et al. (1997), (m) Clough et al. (1997).

Parameter	Value	Units	Cited values	References
$[O_2]^0$	2×10^{-4}	mol L^{-1}		
$[SO_4]^0$	2.8×10^{-3}	mol L^{-1}		
$[NO_3]^0$	1×10^{-5}	mol L^{-1}		
F_{OM1}	2.33×10^{-5}	mol cm^2 yr^{-1}	$(0.8–10)\times10^{-5}$	a, b
F_{OM2}	1.0×10^{-7}	mol cm^2 yr^{-1}		
$F_{Fe(OH)3}$	4×10^{-8}	mol cm^{-2} yr^{-1}		
F_{MnO2}	5.8×10^{-10}	mol cm^{-2} yr^{-1}		
k_{OM1}	0.1	yr^{-1}	0.1–80	c, d, e
k_{OM2}	4×10^{-5}	yr^{-1}	$(5–500)\times10^{-5}$	c, d
C^{lim}_{O2}	8.0×10^{-6}	mol L^{-1}	$(1–30)\times10^{-6}$	f, e
C^{lim}_{NO3}	1.0×10^{-4}	mol L^{-1}	$(2–80)\times10^{-6}$	e
C^{lim}_{MnO2}	1.0×10^{-6}	mol g^{-1}	$(4–32)\times10^{-6}$	e
$C^{lim}_{Fe(OH)3}$	3.0×10^{-6}	mol g^{-1}	$10^{-6}–10^{-4}$	f, e
C^{lim}_{SO4}	1.0×10^{-3}	mol L^{-1}	$10^{-6}–10^{-3}$	f
k_{FeOx}	3.5×10^{10}	cm^3 mol^{-1} yr^{-1}	3.5×10^{10}	f, e
k_{SOx}	1.6×10^{8}	cm^3 mol^{-1} yr^{-1}	1.6×10^{8}	f, e
k_{NH4Ox}	5×10^{9}	cm^3 mol^{-1} yr^{-1}	5×10^{9}	f
k_{SFe3}	4.0×10^{6}	cm^3 mol^{-1} yr^{-1}	$10^{5}–10^{8}$	g, e
k_{SFeCO3}	1.0×10^{7}	cm^3 mol^{-1} yr^{-1}		
k_{FeSOx}	3.0×10^{8}	cm^3 mol^{-1} yr^{-1}	$10^{8}–10^{10}$	h
k_{surFe}	1.25×10^{10}	cm^3 mol^{-1} yr^{-1}	$(0.5–5)\times10^{10}$	f
k_{surMn}	2.5×10^{9}	cm^3 mol^{-1} yr^{-1}	$(0.8–20)\times10^{9}$	f
k_{FeSHS}	0	cm^3 mol^{-1} yr^{-1}		
k_{MnO2S}	2.0×10^{7}	cm^3 mol^{-1} yr^{-1}	$(1–2)\times10^{7}$	f, h
k_{Fe3FeS}	0	g mol^{-1} yr^{-1}		
k_{FeSMn}	0	g mol^{-1} yr^{-1}		
k_{FeMnO2}	3.0×10^{9}	cm^3 mol^{-1} yr^{-1}	$10^{6}–10^{9}$	f, e
k_{FeS}	5.0×10^{-8}	mol g^{-1} yr^{-1}	$10^{-7}–10^{-4}$	f, h
k'_{FeS}	1.0×10^{-3}	yr^{-1}	$10^{-3}–10^{-4}$	f, h
k_{FeCO3}	4.5×10^{-4}	mol g^{-1} yr^{-1}	$(4.5–100)\times10^{-4}$	f
k'_{FeCO3}	0.25	yr^{-1}	0.01–0.25	f
k_{MnCO3}	1.0×10^{-4}	mol g^{-1} yr^{-1}	$(1–100)\times10^{-4}$	f
k'_{MnCO3}	0.25	yr^{-1}	$10^{-2}–10^{3}$	f
K'_{FeCO3}	4×10^{-9}	$(mol\ L^{-1})^2$		f
K'_{MnCO3}	4×10^{-8}	$(mol\ L^{-1})^2$		f
K'_{FeS}	2.51×10^{-3}	mol L^{-1}	$10^{-4}–10^{-3}$	i, j
$K^*_{Fe\_Fe}$	5.0×10^{-7}	—		
$K^*_{Fe\_Mn}$	4.0×10^{-7}	—		
$K^*_{Fe\_B}$	1.0×10^{-8}	—		
$K^*_{Mn\_Fe}$	6.0×10^{-7}	—		
$K^*_{Mn\_Mn}$	6.0×10^{-7}	—		
$K^*_{Mn\_B}$	1.0×10^{-8}	—		
S_{TFe}, S_{TMn}	1.2×10^{-3}	mol g^{-1}		f
S_{TB}	3.3×10^{-6}	mol g^{-1}		f
ρ	2.65	g cm^{-3}		
U	0.001	cm yr^{-1}	10^{-3}	a, k, l
D^0_b	0.1	cm^2 yr^{-1}	0.01–1	d, l, m
pH (x=0)	8.0			
α^0_{irr}	10	yr^{-1}	2–200	d, m
α_1	0.4	cm^{-1}		

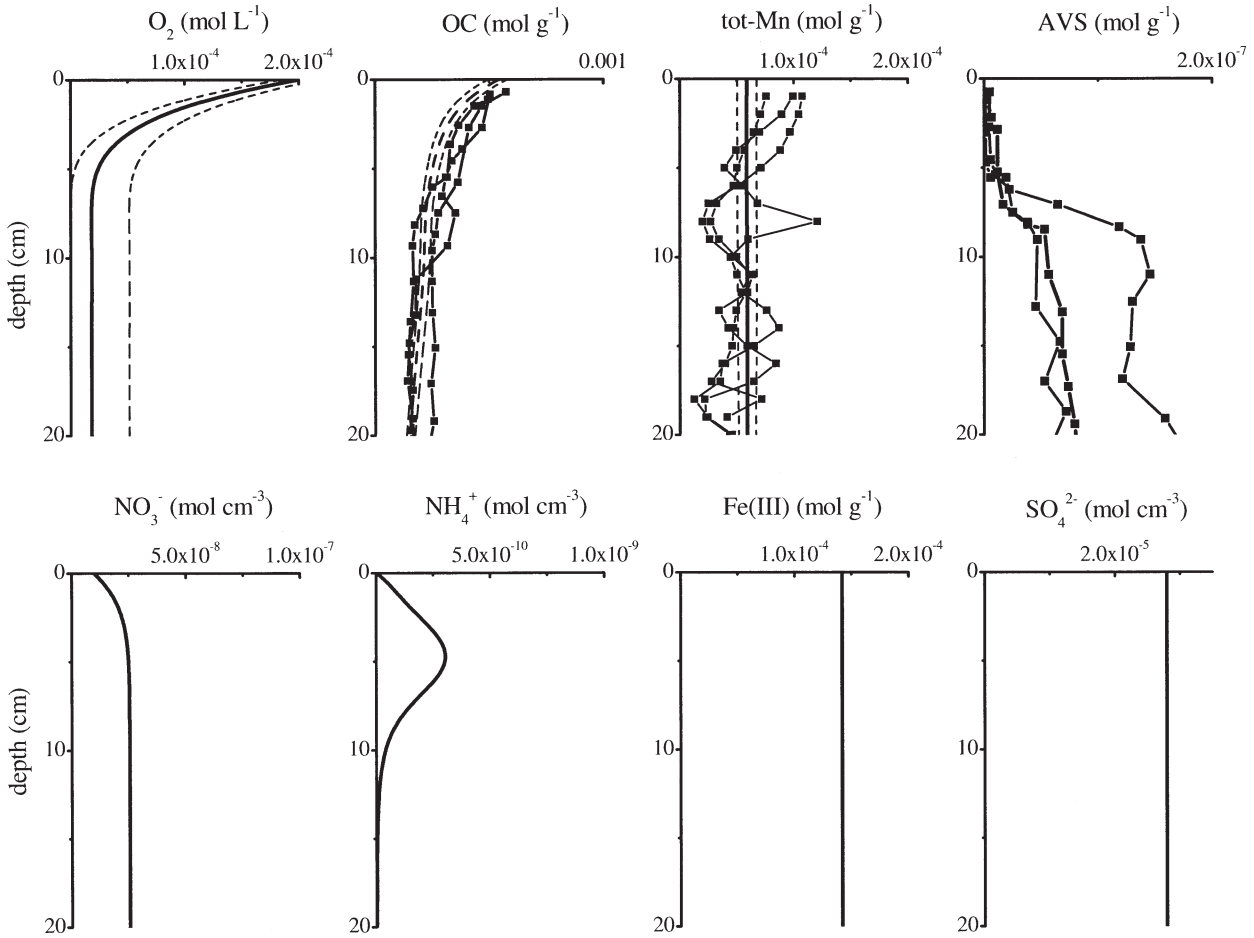

Fig. 2. Steady-state depth profiles and experimental data. Data points indicate measured concentrations for stations 18, 26, and 36 of Gobeil et al. (2001), solid curves are our model solutions. The apparently transient nature of the measured depth profiles (with AVS present) precludes precise calibration for a reference steady state in which oxygen penetrates deep into the sediment (sediment pore-water was undersaturated with respect to FeS in these steady-state solutions). Thus, concentration ranges for OM and tot-Mn, rather than exact profile shapes, were matched. Model sensitivity is indicated by the profile variation ranges (bounded by the dashed lines) that were obtained by randomly and simultaneously varying the parameters F_{OM1}, F_{OM2}, k_{OM1}, k_{OM2}, D_b^0, α_{irr}^0, and $[O_2]^0$ within 10% of their reference values. To sample the model phase space evenly, Halton randomization (Reichert et al. 2002) was used to generate parameter sets for 50 model runs.

absence of a dissolved sulfate concentration gradient (e.g., Wilson et al. 1986).

Formation of peaks in the depth profile of solid-phase Mn—Our simulations reveal that peaks in the depth profile of solid-phase manganese can form diagenetically as a result of an increased flux of organic carbon to the sediment. When fresh organic matter is mixed into the sediment below the redox boundary, reductive dissolution of Mn oxides erodes the profile (Fig. 5). Upward diffusion of soluble Mn(II) and its reprecipitation as an oxide increase the solid-phase Mn concentration above the redox boundary. Adsorption of Mn(II) onto Mn and Fe oxides and precipitation of manganese carbonate result in a small enrichment in solid Mn below the zone of Mn-oxide dissolution (Fig. 5). The ensuing downward migration of the redox boundary can redistribute Mn within the sediment column, shifting the peaks downward (Fig. 5) as manganese dissolves below the redox boundary and precipitates above it. The decrease in the bioturbation coefficient with depth (Fig. 1) also shifts the solid-Mn profile down: Mn-enriched particles that are mixed deep into the sediment are likely to remain buried.

Successive vertical migrations of the redox boundary can generate multiple peaks in the solid-Mn profile (Fig. 6), as well as shift or modify existing Mn distributions. Mn oxides are unaffected during the downward migration of the redox boundary but dissolve behind a rising redox boundary. Because Mn(II) diffusing up from the suboxic and anoxic zones is oxidized and precipitated at the oxidation front, migrations of the redox boundary result in a net upward transport of Mn. Prolonged immobility of the oxic–anoxic front at a particular depth leads to Mn enrichment immediately above it (Burdige in press).

Below the bioturbation zone, the solid manganese distribution remains largely unaffected by redox fluctuations on the selected short time scales of interest because of the low reactivity of organic matter there. If anoxic

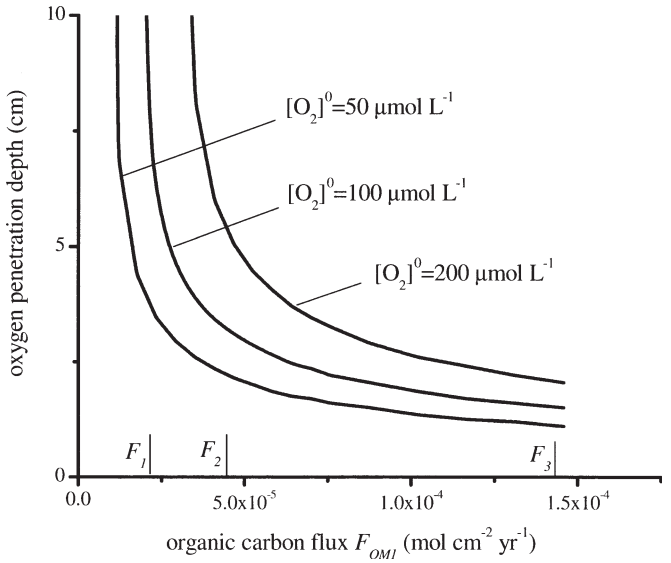

Fig. 3. Steady-state oxygen penetration depth (OPD) as a function of the overlying water oxygen concentration and the sedimentation rate of reactive organic mater. OPD is defined as a depth within the sediment below which $[O_2] < 1\mu$mol L^{-1}.

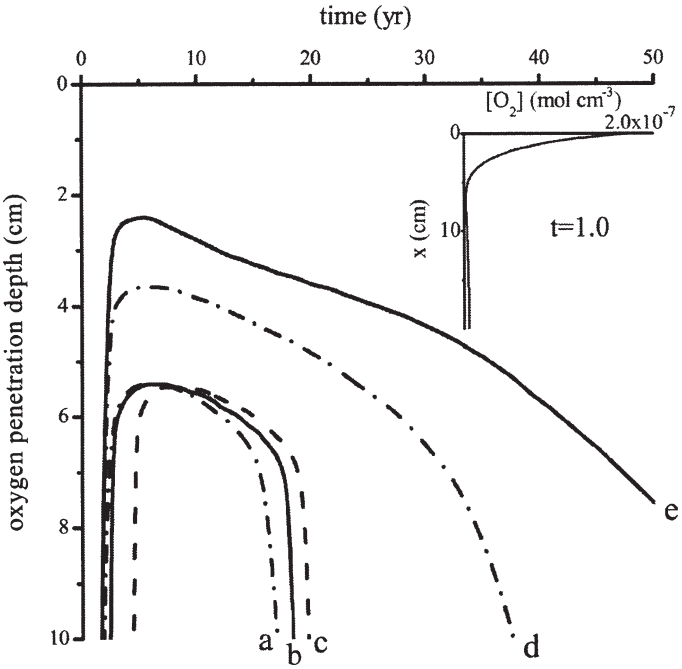

Fig. 4. Temporal evolution of the oxygen penetration depth (OPD) (defined as $[O_2] < 1$ μmol L^{-1}) following an increase at $t = 0$ in the organic matter flux, F_{OM1}, from a steady-state flux F_1 to (a) $49F_1$ for 1 month, (b) $5F_1$ for 1 yr, (c) $2F_1$ for 4 yr, (d) $10F_1$ for 1 yr, (e) $10F_1$ for 2 yr. Note that the total amount of organic carbon deposited in excess of the steady-state flux is the same for cases (a), (b), and (c). The inset shows the pore-water oxygen concentration profile at $t = 1.0$ yr for case (d).

conditions prevail long enough to allow complete reduction of the Mn oxides by the more refractory organic matter buried below the bioturbation zone (on the time scale of thousands of years), the reactive manganese is either transported to the interface or immobilized in the reduced sediment by adsorption or carbonate precipitation.

Ultimately, the distribution of solid-phase Mn depends both on the history of the redox boundary position and on prior Mn distributions (Fig. 6, *see* caption). The profiles in Fig. 6 were obtained by starting the simulations from a steady state characterized by oxidized manganese concentrations that were nearly constant within a fully oxic sediment column (Fig. 2). Different initial conditions would not alter our conclusions but would affect such details of the transient profiles as the positions and magnitudes of the peaks.

Multiple peaks in the depth profiles of redox-sensitive elements were previously interpreted as accumulation of upward-diffusing Mn(II), following a redox boundary migration (e.g., Mangini et al. 2001). For typical Mn(II) fluxes, such accumulation requires time scales greater than $\sim 10^2$–10^3 yr, such as those associated with glacial/interglacial transitions or Holocene variations in the organic carbon rain rate (Burdige in press, and references therein). In contrast, the Mn profiles in Fig. 6 are formed on a time scale of decades by diagenetic redistribution of Mn within the sediment. The rate of this redistribution is limited mainly by the migration rate of the redox boundary because manganese reduction by fresh organic matter is rapid (Myers and Nealson 1988). Formation of multiple Mn peaks on such a short time scale requires several conditions. First, a sufficient amount of oxidized manganese should be present over the entire depth range in the sediment column where peaks are to form (10 s of cm). Second, reactive organic matter should be mixed into the sediment to provide the necessary reducing capacity. And third, the redox boundary should shift by at least several centimeters in order to generate a centimeter-scale peak pattern. Our results suggest that all of these conditions can be encountered in deep Arctic Ocean sediments.

Scenarios for redox boundary migration in deep Arctic sediments—To determine the type of event that could be responsible for the recent migration(s) of the redox boundary in deep Arctic Ocean sediments (Gobeil et al. 2001), we simulated the response of sediment to several scenarios of variable organic carbon input (short single events, gradual increase in F_{OM1}, repetitive events, and combinations of these). These scenarios are represented schematically in Fig. 7. The results are summarized in Table 4, and sample parameterizations for each scenario are specified in the table caption. All scenarios resulted in qualitatively similar depth profiles for dissolved oxygen and total solid-phase manganese (Figs. 5 and 6). The simulated profiles of solid-phase Mn were consistent with those observed by Gobeil et al. (2001): both measured and simulated profiles display a near-surface enrichment of Mn and a smaller peak about 10 cm below the sediment–water interface. Whenever AVS precipitation occurred, its distri-

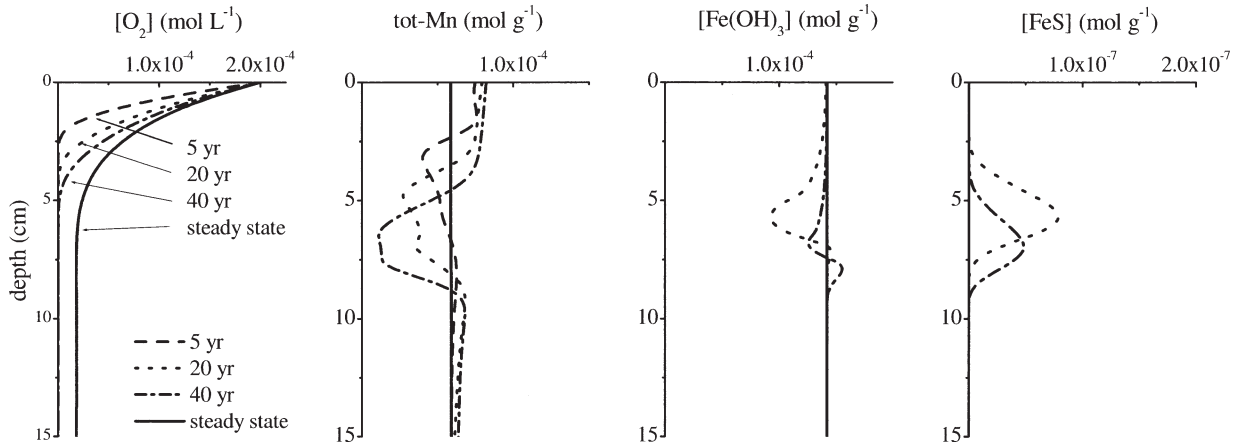

Fig. 5. Simulated depth profiles for selected sediment species at different times during a redox boundary excursion. The steady-state profiles shown as a solid line were used as initial conditions for transient solutions. At $t = 0$, the flux of reactive organic carbon F_{OM1} was increased 10-fold for a period of 2 yr (case (e) in Fig. 4).

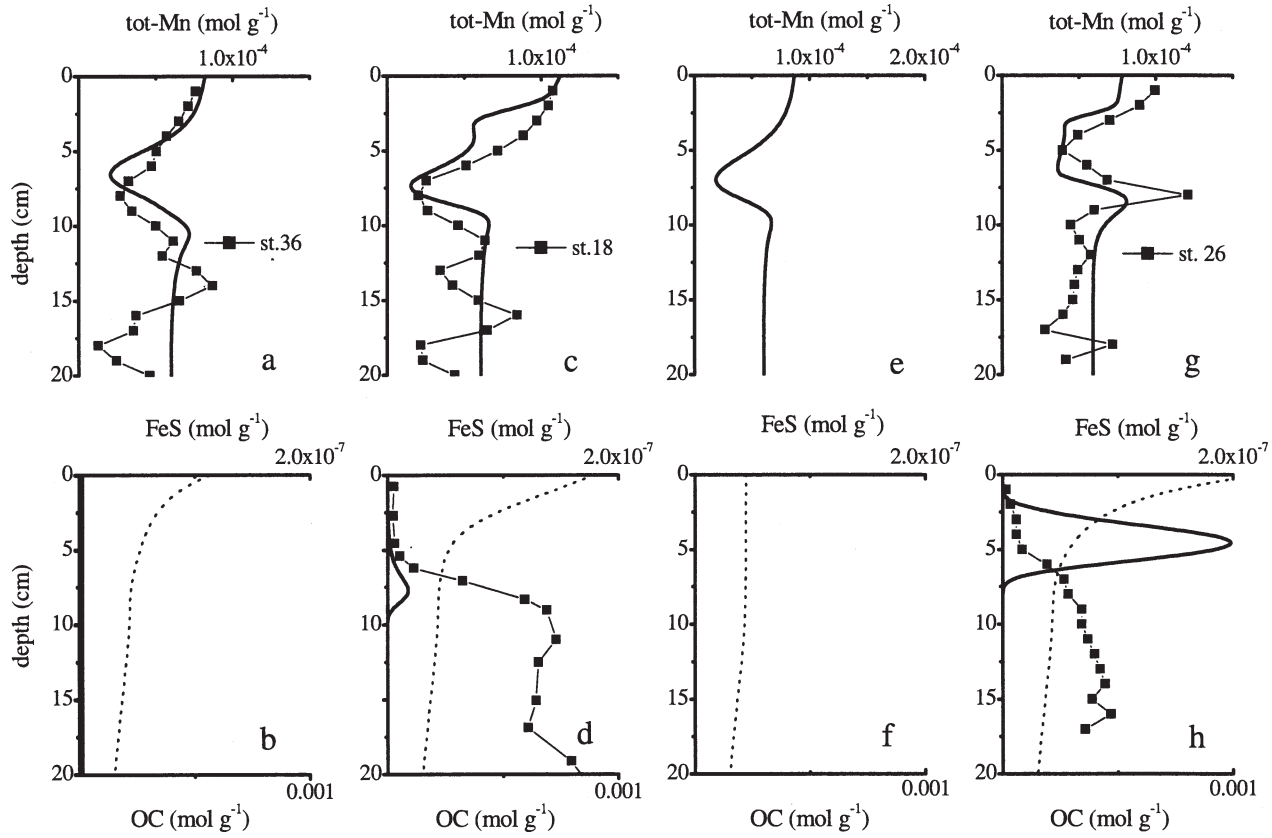

Fig. 6. The effect of multiple redox boundary oscillations on the solid Mn and AVS profiles. All profiles were obtained starting from a fully oxic steady state described by the parameter set in Table 3. Data points of Gobeil et al. (2001) are superimposed on the simulated profiles for illustration. Dotted lines indicate organic carbon concentrations within the sediment. The steady-state OM sedimentation flux is F_1. (a, b) F_{OM1} was set to $10F_1$ for 1 yr and the event was repeated at 50-yr intervals (scenario 1 in Fig. 7). The profile was recorded at $t = 70$ yr. (c, d) F_{OM1} was set to $10F_1$ for 2 yr and the event was repeated at 40-yr intervals (scenario 2 in Fig. 7). The profile was recorded at $t = 45$ yr. (e, f) F_{OM1} repeatedly and linearly oscillated between F_1 and $1.5F_1$ over 50-yr intervals (scenario 3 in Fig. 7). The profile was recorded at $t = 80$ yr. (g, h) F_{OM1} increased linearly fourfold over 35 yr (scenarios 4 and 5 in Fig. 7).

bution below the oxygen penetration depth was bell shaped, with maximum concentration on the order of 10^{-7} mol g^{-1}, consistent with the AVS concentrations reported by Gobeil et al. (2001).

Because of the similarity of the generated profiles and the scant amount of field data, we could not discriminate between the organic-matter loading scenarios and the rates of redox boundary migration that are associated with them. We can, however, rule out large seasonal excursions of the redox boundary (c.f. Soetaert et al. 1996; Glud et al. 2003). As Figure 4 illustrates, the upward migration of the redox boundary and the subsequent penetration of oxygen to below 10–20 cm require several years. The time for the upward migration is comparable with $1/k_{OM1} = 10$ yr (Martin and Bender 1988) because a large fraction of the freshly deposited organic carbon must be mineralized before the redox boundary can move. The redox boundary is thus unlikely to respond to seasonal variations in the OM input in situations where organic carbon reactivity is low (Sayles et al. 1994). In addition, when anoxic conditions last long enough to allow for precipitation of AVS in quantities such as those observed in the sediment cores shown in Fig. 2, reduced substances accumulate within the sediment column, delaying the downward penetration of oxygen (Fig. 4). For these reasons, the depth profiles generated in our simulations are essentially identical between scenario 4 (i.e., seasonally modulated OM flux; Fig. 7) and scenario 5 (i.e., seasonally averaged OM flux). Figure 8 illustrates seasonal OPD migrations about a steady state. In this simulation, the flux of organic carbon varies seasonally by more than an order of magnitude, yet the resulting redox boundary displacements are limited to a few millimeters (Fig. 8a). In contrast, oxygen concentration in the bottom water has a much stronger effect on the redox boundary position (Fig. 8b).

The accumulation of AVS in concentrations observed in deep basin Arctic sediments does not necessarily require a long-established anoxia, as Fig. 6d,h illustrates. This point can be also made with a time-scale argument. AVS precipitation requires that anoxic conditions persist long enough for both iron and sulfate reduction to take place. Mn reduction, which is thermodynamically more favorable (Froelich et al. 1979), should precede these reactions. If we assume, as an order-of-magnitude estimate, that the rate of sulfate reduction after an episodic increase in OM loading is 1% of the total organic-matter degradation rate, that the concentration of reactive organic matter, [OM1], is 10^{-4} mol (g dry wt) $^{-1}$, that the rate constant k_{OM1} is 0.1 yr^{-1}, and that the stoichiometry of the sulfate reduction reaction is given by reaction 5 (Table 1), then enough sulfide to precipitate 10^{-7} mol (g dry wt)$^{-1}$ of FeS can be produced in as little as 2 yr. In our simulations, the amount of precipitated FeS depends on the rate and magnitude of the organic matter flux increase but, typically, a FeS concentration 10^{-7} mol g^{-1} (the order of magnitude reported by Gobeil et al. [2001]) can be achieved within several years after the sediment becomes anoxic.

The distribution of AVS within the sediment column, however, imposes a stricter constraint on the minimum duration of anoxia. The AVS profiles in the Arctic sediment cores of Gobeil et al. (2001) are bell shaped, with significant AVS concentrations down to a depth of 40 cm. Assuming that reducing conditions result from a relatively recent increase in the organic carbon flux to the seafloor, and that the fresh organic matter is mixed into the sediment by bioturbation, the three reductive processes (Mn, Fe, and SO_4 reduction) should mainly be limited to the depth range that is influenced by bioturbation. The reduction of Mn(IV), Fe(III), and SO_4 should be much slower below the bioturbated layer because of the lower reactivity of the organic matter there, and precipitation of FeS should be negligible. Therefore, the presence of AVS to 30–40 cm depth is enigmatic.

We can offer two alternative explanations for the presence of AVS at depth. The sediment may have been anoxic for a sufficiently long time to allow the downward transport of AVS by burial. Given a sedimentation rate of about 1 cm per 1,000 yr (Schneider et al. 1996), this explanation implies that deep basin Arctic sediments have been anoxic below the bioturbation depth for several

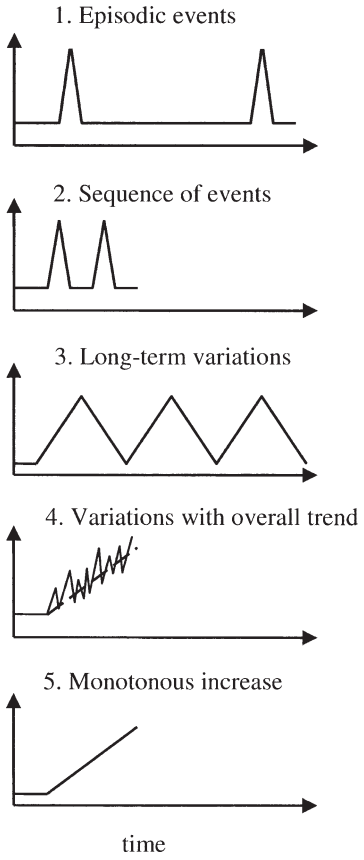

Fig. 7. Selected scenarios of the temporal variability in degradable organic carbon deposition fluxes. (1) Episodic sedimentation events. The sediment is completely reoxidized between the events. (2) Pulses of organic matter occur at short intervals that do not allow complete reoxidation of the sediment. (3) Slow (e.g., over decades or centuries) variation in the organic C flux. (4) Stochastic (e.g., seasonal) variations in organic C flux with an overall increasing trend. (5) Continuous, monotonous increase in organic C flux.

Table 4. Sediment responses to different scenarios of organic carbon loading. Notation: √ = yes, — = no. The following conditions were used to characterize the increase in F_{OM1} from its steady-state value $F_{OM1} = F_1$ (Table 3) for each of the scenarios (*see* also Fig. 7) up to a maximum simulation time t_{max}: (1) F_{OM1} increased to $10F_1$ for 1 yr (*see* also Fig. 4). The event was repeated after 50 yr, t_{max}=100 yr. (2) F_{OM1} increased to $10F_1$ for 2 yr. The event was repeated twice at 40-yr intervals, t_{max}=100 yr. (3) F_{OM1} increased and decreased linearly 1.5-fold over 50-yr time intervals, t_{max}=250 yr. (4) $F_{OM1}(t)$ exhibited a (summer) peak described by a Gaussian bell curve with characteristic (4-sigma) width of 1 month and maximum amplitude $A \times F^{win}$, where A=20 and F^{win} is the winter flux. F^{win} was calculated so that a running 1-yr average value for $F_{OM1}(t)$ increased linearly from F_1 at t=0 to $4F_1$ at t_{max}=50 yr. (5) F_{OM1} increased linearly fourfold over t_{max}=50 yr.

	Scenarios (see Fig. 7)				
Sediment response	1	2	3	4	5
OPD migrates from infinity to near interface	√	√	√	√	√
AVS formation in bioturbation zone	—	√	—	√	√
AVS in deep sediment (below bioturbation)	—	—	—	—	—
Enrichment in solid Mn near interface	√	√	√	√	√
Multiple peaks in solid Mn	√	√	√	√	√
Diagenetic migration of Mn peak down	√	√	√	√	√
OPD reaches infinity between events	√	—	√	N/A	N/A
Precipitation of Mn carbonate	—	√	√	—	√
Precipitation of Fe carbonate	—	√	√	√	√

millennia. If so, one has to account for the high levels of solid-phase manganese in this sediment. The speciation of this manganese is not known; it can consist of Mn oxides and reduced phases, such as Mn carbonates and Mn(II) sorbed or coprecipitated with a variety of sediment solids. It is conceivable that solid-phase Mn oxide could have survived in the reduced sediment for several centuries, or even millennia, given the refractory nature of the organic matter that is buried below the bioturbation zone (typical rate constant k_{OM2} = (5–500) × 10^{-5} yr^{-1}, Table 3). Taken together, these arguments support the possibility that deep Arctic sediments have been anoxic for several millennia, but they are not consistent with the idea of a recent upward migration of the redox boundary. An alternative explanation, which is consistent with substantial migrations of the redox boundary on short time scales, is that iron and sulfate reduction below the bioturbated layer is supported, not by refractory organic matter, but by dissolved organic matter produced in the bioturbated layer during episodes of increased input of fresh organic carbon.

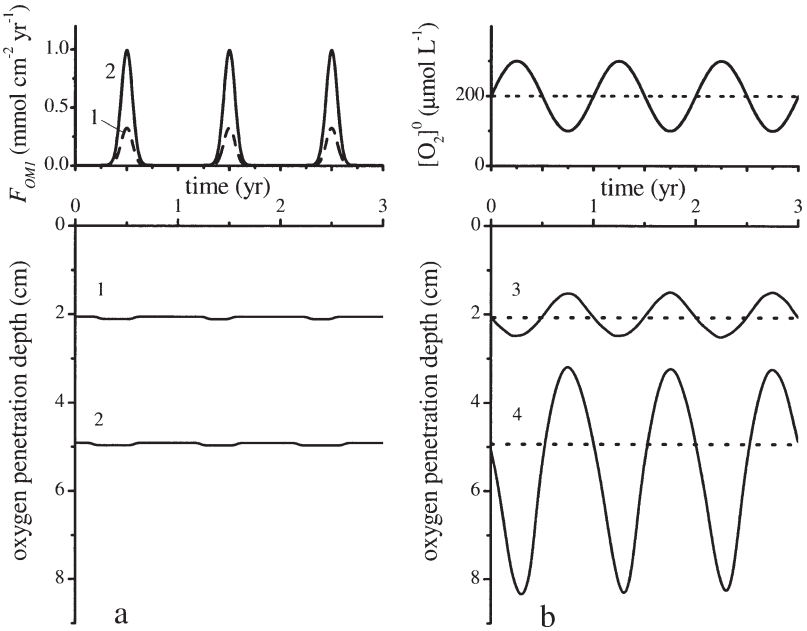

Fig. 8. Migrations of the redox boundary in response to (a) seasonal variations in organic matter input and (b) bottom water oxygen concentration. (a) F_{OM1} fluctuates seasonally as shown at the top so that its seasonal average corresponds to (1) F_2 in Fig. 3; (2) F_3 in Fig. 3. (b) $[O_2]^0$ varies sinusoidally as shown at the top with an amplitude of 50% of its reference value, 200 μmol L^{-1}. F_{OM1} is constant and equal to (3) F_2; (4) F_3. Steady-state OPD values are marked with a dotted line.

Diffusion of dissolved organic matter in sediment porewater is rapid, and long periods of anoxia are not required to produce AVS below the bioturbated layer. This hypothesis, which couples AVS accumulation within and below the bioturbated layer to episodic inputs of organic matter, could not be tested with the present model.

In summary, we charted the position and migration rates of the redox boundary in sediment as a function of the flux of organic carbon to the seafloor and bottom-water oxygen concentration. In organic-poor sediments (such as in the deep Arctic Ocean basins), the position of the redox boundary is highly susceptible to changes in the carbon flux to the seafloor: relatively small and/or brief increases in the organic carbon flux can cause the redox boundary to migrate from deep within the sediment to a few cm from the sediment–water interface. Such migrations can generate peaks in the depth distributions of redox-sensitive elements, such as manganese, on time scales of years and decades. Seasonal variations in the depth of oxygen penetration in these sediments are expected to be negligible. The model simulations support the hypothesis of Gobeil et al. (2001) that the sediments in the deep basins of the Arctic Ocean have experienced a rapid and recent upward migration of the redox boundary over a period of several decades as a result of increased water column productivity.

References

Belicka, L. L., R. W. MacDonald, and H. R. Harvey. 2002. Sources and transport of organic carbon to shelf, slope, and basin surface sediments of the Arctic Ocean. Deep Sea Res. I **49:** 1463–1483.

Benoit, P., Y. Gratton, and A. Mucci. In press. Modeling of dissolved oxygen levels in the bottom waters of the Lower St. Lawrence Estuary: Coupling of benthic and pelagic processes. Mar. Chem.

Berg, P., S. Rysgaard, and B. Thamdrup. 2003. Dynamic modeling of early diagenesis and nutrient cycling. A case study in an Arctic marine sediment. Am. J. Science **303:** 905–955.

Berner, R. A. 1980. Early diagenesis: A theoretical approach. Princeton series in geochemistry, Princeton Univ. Press.

Boudreau, B. P. 1997. Diagenetic models and their implementation. Springer.

———, A. Mucci, B. Sundby, G. W. Luther, and N. Silverberg. 1998. Comparative diagenesis at three sites on the Canadian continental margin. J. Mar. Res. **56:** 1259–1284.

Brown, P. N., G. D. Byrne, and A. C. Hindmarsh. 1989. VODE, a variable-coefficient ODE solver: SIAM J. Sci. Stat. Comput. **10:** 1038–1051.

Burdige, D. J. 1993. The biogeochemistry of manganese and iron reduction in marine sediments. Earth Sci. Rev. **35:** 249–284.

———. 2006. Geochemistry of marine sediments. Princeton Univ. Press, Princeton.

Carignan, R., and D. R. S. Lean. 1991. Regeneration of dissolved substances in a seasonally anoxic lake: The relative importance of processes occurring in the water column and in the sediments. Limnol. Oceanogr. **36:** 683–707.

Carlton, R. G., and R. G. Wetzel. 1988. Phosphorus flux from lake sediments: Effect of epipelic algal oxygen production. Limnol. Oceanogr. **33:** 562–570.

Clough, L. M., W. G. Ambrose, Jr., J. K. Cochran, C. Barnes, P. E. Renaud, and R. C. Aller. 1997. Infaunal density, biomass and bioturbation in the sediments of the Arctic Ocean. Deep Sea Res. II **44:** 1683–1704.

Fossing, H., P. Berg, B. Thamdrup, S. Rysgaard, H. M. Sorensen, and K. Nielsen. 2004. A model set-up for an oxygen and nutrient flux model for Aarhus Bay (Denmark). NERI Technical Report, No. 483 (Denmark).

Froelich, P. N., G. P. Klinkhammer, M. L. Bender, G. R. Luedtke, G. R. Heath, D. Cullen, and P. Dauphin. 1979. Early oxidation of organic matter in pelagic sediments of the eastern equatorial Atlantic: Suboxic diagenesis. Geochim. Cosmochim. Acta **43:** 1075–1090.

Gehlen, M., C. Rabouille, U. Ezat, and L. D. Guidi-Guilvard. 1997. Drastic changes in deep-sea sediment porewater composition induced by episodic input of organic matter. Limnol. Oceanogr. **42:** 980–986.

Glud, R. N., J. K. Gundersen, H. Roy, and B. B. Jorgensen. 2003. Seasonal dynamics of benthic O_2 uptake in a semienclosed bay: Importance of diffusion and faunal activity. Limnol. Oceanogr. **48:** 1265–1276.

Gobeil, C., R. W. MacDonald, and B. Sundby. 1997. Diagenetic separation of Cd and Mn in suboxic continental margin sediments. Geochim. Cosmochim. Acta **61:** 4647–4654.

———, B. Sundby, R. W. MacDonald, and J. N. Smith. 2001. Recent change in organic carbon flux to Arctic Ocean deep basins: Evidence from acid volatile sulfide, manganese and rhenium discord in sediments. Geophys. Res. Lett. **28:** 1743–1746.

Hargrave, B. T., I. D. Walsh, and D. W. Murray. 2002. Seasonal and spatial patterns in mass and organic matter sedimentation in the North Water. Deep Sea Res. II **49:** 5227–5244.

Hunter, K. S., Y. Wang, and P. Van Cappellen. 1998. Kinetic modeling of microbially-driven redox chemistry of subsurface environments: Coupling transport, microbial metabolism and geochemistry. J. Hydrol. **209:** 53–80.

Jung, M., J. Ilmberger, A. Mangini, and K.-C. Emeis. 1997. Why some Mediterranean sapropels survived burn-down (and others did not). Mar. Geol. **141:** 51–60.

Katsev, S., D. G. Rancourt, and I. L'Heureux. 2004. dSED: A database tool for modeling sediment early diagenesis. Comput. Geosci. **30:** 959–967.

Mangini, A., A. Eisenhauer, and P. Walter. 1991. A spike of CO_2 in the atmosphere at glacial–interglacial boundaries induced by rapid deposition of manganese in the oceans. Tellus **43B:** 97–105.

———, M. Jung, and S. Laukenmann. 2001. What do we learn from peaks of uranium and of manganese in deep sea sediments? Mar. Geol. **177:** 63–78.

Martens, C. S., and J. V. Klump. 1984. Biogeochemical cycling in an organic-rich coastal marine basin 4. An organic carbon budget for sediments dominated by sulfate reduction and methanogenesis. Geochim. Cosmochim. Acta **48:** 1987–2004.

Martin, W. R., and M. L. Bender. 1988. The variability of benthic fluxes and sedimentary remineralization rates in response to seasonally variable organic carbon rain rates in the deep sea: A modeling study. Am. J. Sci. **288:** 561–574.

Mendelssohn, I. A., B. A. Kleiss, and J. S. Wakeley. 1995. Factors controlling the formation of oxidized root channels: A review. Wetlands **15:** 37–46.

Middelburg, J. J., K. Soetaert, and P. M. J. Herman. 1997. Empirical relationships for use in global diagenetic models. Deep Sea Res. I **44:** 327–344.

Millero, F. J. 1995. Thermodynamics of the carbon dioxide system in the oceans. Geochim. Cosmochim. Acta **59:** 661–677.

Morse, J. W., F. J. Millero, J. C. Cornwell, and D. Rickard. 1987. The chemistry of the hydrogen sulfide and iron sulfide systems in natural waters. Earth Sci. Rev. **24:** 1–42.

Myers, C. R., and K. H. Nealson. 1988. Microbial reduction of manganese oxides: Interactions with iron and sulfur. Geochim. Cosmochim. Acta **52:** 2727–2732.

Reichert, P., M. Schervish, and M. J. Small. 2002. An efficient sampling technique for Bayesian inference with computationally demanding models. Technometrics **44:** 318–427.

Sayles, F. L., W. R. Martin, and W. G. Deuser. 1994. Response of benthic oxygen-demand to particulate organic-carbon supply in the deep-sea near Bermuda. Nature **371:** 686–689.

Schaller, T., H. C. Moor, and B. Wehrli. 1997. Sedimentary profiles of Fe, Mn, V, Cr, As and Mo as indicators of benthic redox conditions in Baldeggersee. Aquat. Sci. **59:** 345–361.

Schneider, D. A., J. Backman, W. B. Curry, and G. Possnert. 1996. Paleomagnetic constraints on sedimentation rates in the Eastern Arctic Ocean. Quaternary Res **46:** 62–71.

Soetaert, K., P. M. J. Herman, and J. J. Middelburg. 1996. Dynamic response of deep-sea sediments to seasonal variations: A model. Limnol. Oceanogr. **41:** 1651–1668.

Soltwedel, T., V. Mokievsky, and I. Schewe. 2000. Benthic activity and biomass on the Yermak Plateau and in adjacent deep-sea regions northwest of Svalbard. Deep Sea Res. I **47:** 1761–1785.

Stumm, W., and J. J. Morgan. 1996. Aquatic chemistry: Chemical equilibria and rates in natural waters, 3rd ed. John Wiley.

Sundby, B., C. Vale, M. Caetano, and G. W. Luther III. 2003. Redox chemistry in the root zone of a salt marsh sediment in the Tagus Estuary, Portugal. Aquatic Geochem **9:** 257–271.

Thomson, J., N. C. Higgs, and S. Colley. 1996. Diagenetic redistributions of redox-sensitive elements in northeast Atlantic glacial/interglacial transition sediments. Earth Planet. Sci. Lett. **139:** 365–377.

Tromp, T. K., P. Van Cappellen, and R. M. Key. 1995. A global model for the early diagenesis of organic carbon and organic phosphorus in marine sediments. Geochim. Cosmochim. Acta **59:** 1259–1284.

Van Cappellen, P., and Y. Wang. 1996. Cycling of iron and manganese in surface sediments: A general theory for the coupled transport and reaction of carbon, oxygen, nitrogen, sulfur, iron, and manganese. Am. J. Sci. **296:** 197–243.

Wilson, T. R. S., J. Thomson, D. J. Hydes, S. Colley, F. Culkin, and J. Sorensen. 1986. Oxidation fronts in pelagic sediments: Diagenetic formation of metal-rich layers. Science **232:** 972–975.

Received: 15 September 2005
Accepted: 29 December 2005
Amended: 23 January 2006